


Phase-field modeling of the morphological evolution of ringlike structures during growth: Thermodynamics, kinetics, and template effects

Marcello De Donno ^{*}, Marco Albani , Roberto Bergamaschini [†] and Francesco Montalenti 
L-NESS and Department of Materials Science, Università di Milano-Bicocca, 20125 Milano, Italy

 (Received 23 July 2021; revised 9 November 2021; accepted 27 January 2022; published 11 February 2022)

Understanding and controlling the morphology of crystals growing from prepatterned shapes, as in selective-area epitaxy, is fundamental for the development of novel device architectures. Here, an in-depth analysis of the faceted growth of ring-shaped crystal structures is presented. This is a prototypical case for assessing the role of thermodynamic and kinetic driving forces, as they induce different faceting between the outer convex region and the inner concave one. The well-established concepts of equilibrium crystal shape, set by surface energy minimization, and its kinetic counterpart, determined by orientation-dependent growth rates, provide a qualitative indication of the outcome of growth experiments. However, they are insufficient to capture the whole evolution pathway. A phase-field growth model including deposition, incorporation, and surface diffusion dynamics is considered, and extensive two- and three-dimensional simulations are performed. A continuum transition in the crystal morphology is recognized by varying the magnitude of the anisotropic surface energy vs the incorporation times. The in-depth analysis of a realistic case, mimicking experiments in the literature, highlights the prominent role of kinetics and of material redistribution from the outer to the inner perimeter of the ring. Finally, the templating effect of the initial pattern is investigated by considering polygonal profiles with different orientations, showing their effect on the facet formation and evolution.

DOI: [10.1103/PhysRevMaterials.6.023401](https://doi.org/10.1103/PhysRevMaterials.6.023401)

I. INTRODUCTION

The development of next-generation devices at the micro- and nanoscale depends on the improvements in the techniques of epitaxial growth and lithography. The ability to grow three-dimensional (3D) nanostructures of controllable shape and size is of prime importance in the development of new designs, beyond the conventional planar technology. To this purpose, a convenient approach is offered by selective-area epitaxy (SAE), which proved successful in directing the growth of multifarious structures [1], ranging from dots [2,3], columns and nanowires [4–6], and nanomembranes and fins [7–12] up to micrometer-sized crystals. Recently, more complex patterns involving intersecting slits to form crosses [13,14] or networks [15,16] have been considered. Ringlike structures have been grown for GaN [17–20] and InP [10].

The lithographed openings in the protective mask set the initial shape of the growing structures, but as deposition continues and there is crystal overgrowth on top of the mask, its morphology evolves depending on the relative stability and growth rates of the characteristic crystallographic facets. The final outcomes may be radically different, depending not only on the choice of materials, but also on the orientation of the substrate [4,19] and the alignment of the mask openings [10,21], as well as their shape and size [10]. In some cases, the purpose is to exploit the confinement provided by the mask

to maximize the vertical growth and achieve high-aspect-ratio 3D structures (e.g., for nanowires or fins). Vice versa, epitaxial lateral overgrowth (ELO) experiments can be devised to prominently spread the crystal out on top of the mask by enhancing the growth of side facets, eventually filling large areas after coalescence between different seeded regions. This latter approach can be used to improve the crystal quality or, recently, as a strategy to obtain wide regions of a metastable phase favorably initiated within the windows [13].

Accurate tuning of the growth parameters is required to achieve the desired results. First, the temperature and precursor fluxes must be set in a way to ensure selective growth within the mask windows only [11]. Then, once the range of compatible parameters is identified, a finer tuning to balance temperature and growth rate is needed in order to precisely control the crystal shape and morphology.

Physically, the origin of the observed crystal faceting can be ascribed to both thermodynamic and kinetic driving forces [22]. The former sets the equilibrium crystal shape (ECS), i.e., the one formed by the most stable facets returning the minimum surface energy. The latter relates the facet extension to their relative growth rates, leading to the so-called kinetic crystal shape (KCS), eventually dependent on the actual growth technique and parameters, and generally different from the ECS. Both ECS and KCS can be traced by the Wulff construction method [23,24], by considering the orientation dependency of surface energy density γ and growth velocities, respectively. Typically, SAE operates under far-from-equilibrium conditions, so that kinetic factors are relevant, and possibly dominant. Assessing the relative strength of the kinetic and the energetic contributions is difficult, as

^{*}Present address: Institute of Scientific Computing, Technische Universität Dresden, 01062 Dresden, Germany.

[†]roberto.bergamaschini@unimib.it

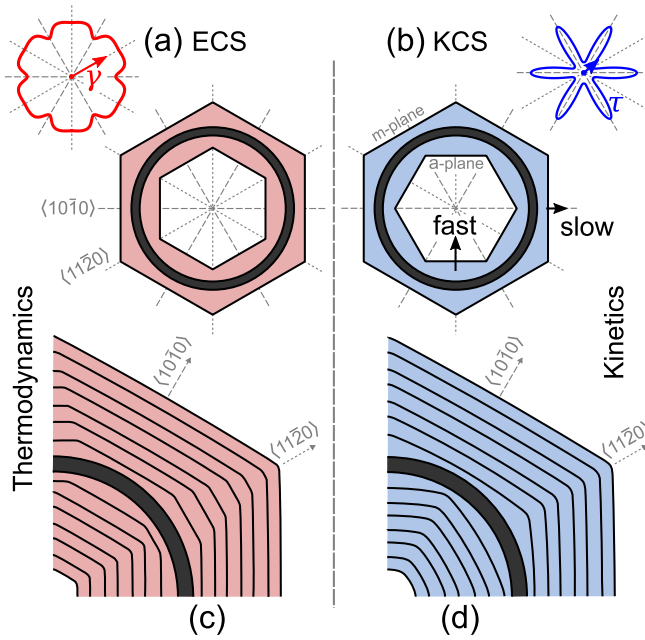


FIG. 1. Growth of a ring (black) with anisotropy only in the energetic term (a) or only in the kinetic term (b). Evolution profiles equally spaced in time are traced in (c) and (d) on quarter systems for the thermodynamic and kinetic evolution, respectively.

they both compete in defining the crystal morphology observed in the experiments. Ideally, one could take the ECS as a reference, known from first-principles calculations of surface energy density or inferred experimentally by carefully exploiting close-to-equilibrium processes, such as high-temperature annealing.

A special case is that of crystal structures including both convex and concave regions, such as rings. If the faceting is driven by thermodynamics, the same low-energy facets are observed in both regions, as exemplified in Fig. 1(a). Vice versa, under kinetic growth conditions, the appearance and extent of each facet are determined by its relative growth velocity (proportional to the local deposition rate Φ and inversely to the adatom-incorporation time τ) with respect to the neighboring ones with an opposite result in convex and concave regions, as shown in Fig. 1(b). In the former case, the slow-growing facets dominate as the profile is expanding. In the latter, fast-growing orientations develop as the profile is contracting. This is a purely geometric effect, codified by the Borgstrom construction [25,26]. For this reason, in ringlike structures it is possible to distinguish whether the faceting results from thermodynamic or kinetic driving forces, by checking whether or not the facets in the convex and concave regions are the same. In Ref. [10] the morphology of InP rings grown by SAE is investigated: $\{10\bar{1}0\}$ and $\{11\bar{2}0\}$ facets are found in the outer perimeter, while the inner one is bounded by 12 intermediate high-index planes. According to the previous analysis, we can infer that kinetic effects are playing a key role during growth, as it is expected that the intermediate orientations are not energetically convenient, but appear because of their high growth rate. Similar considerations were drawn for SAE of GaN structures in Refs. [17–20]. The same

behavior was also found for growth and etching experiments on graphene, a 2D structure, with respect to the edge kinetics [27] recently demonstrated at the atomistic scale by kinetic Monte Carlo simulations [28].

While the widely used concepts of ECS and KCS are helpful for qualitative considerations, they are insufficient to inspect the evolution of the crystal morphology during growth, as it stems from a complex interplay of material deposition, facet-dependent incorporation of adatoms, and redistribution via surface diffusion dynamics, making the crystal morphology dependent on the actual growth conditions. In this paper, we investigate this dynamical behavior for ringlike structures, by exploiting a phase-field growth model [29,30] accounting for both anisotropic surface energy density and facet-dependent adatom kinetics to inspect their relative role and provide a comprehensive characterization of the facet competition between convex and concave regions.

The paper is organized as follows. First, in Sec. II we review the key features of the model and the parameter set considered for the simulations. Then, in Sec. III A we systematically analyze the variation in the crystal faceting when changing the relative strength of surface energy, kinetic incorporation times, and deposition, and characterize the mixed behavior in between ECS and KCS. An in-depth characterization of the faceting of ringlike structures mimicking experiments is then considered in Sec. III B. Finally, in Sec. III C the possibility of controlling the growth morphology by templating it through a suitable shaping and alignment of the mask windows is discussed.

II. METHODS

The phase-field model detailed in Ref. [30] is exploited for simulating the evolution of the crystal morphology during growth. Here, we summarize its key aspects while referring the reader to a previous work [30] for an in-depth description and more technical details.

The system geometry is represented implicitly by an order parameter, i.e., the phase-field function φ , set equal to 1 in the solid phase and 0 in the surrounding gas or liquid phase. The crystal surface is identified by a diffuse interface with a finite thickness $\sim\epsilon$ between the two bulk phases. In the following we will identify the nominal surface profile as the $\varphi = 0.5$ isoline.

The advancing of the growth front, implicitly described by the temporal variation of the phase field $\partial\varphi/\partial t$, is determined by the combined effect of material deposition, arriving at the surface with a local flux Φ , and its redistribution over the surface (bulk diffusion is assumed to be negligible at the growth temperature). According to the Onsager linear law, the diffusion current is proportional to the local gradient of the chemical potential μ . Following Ref. [31], μ comprises both an equilibrium term, given by definition as the variation in free energy F , and a kinetic term, proportional to the profile velocity via a coefficient τ accounting for the (facet dependent) adatom-incorporation time. This simplified description presumes a nucleationless growth process thus restricting the range of applicability to conditions returning nonsingular, kinetically rough facets which look appropriate for a large part of SAE experiments.

The resulting set of partial differential equations (PDEs) reads

$$\begin{cases} \frac{\partial \varphi}{\partial t} = \nabla \cdot [M(\varphi)\nabla \mu] + \Phi(\hat{\mathbf{n}})|\nabla \varphi| \\ g(\varphi)\mu = \frac{\delta F}{\delta \varphi} + \epsilon \tau(\hat{\mathbf{n}})\frac{\partial \varphi}{\partial t}, \end{cases} \quad (1)$$

where $\hat{\mathbf{n}}$ is the outward-pointing surface normal, $g(\varphi) = 30\varphi^2(1-\varphi)^2$ is a stabilizing function [32–34], and $M(\varphi) = M_0(36/\epsilon)\varphi^2(1-\varphi)^2$ is the mobility function restricted to the surface, with M_0 being a scaling factor.

Here, the system free energy F consists only of (anisotropic) surface energy, as a function of the surface energy density γ . Then, μ takes the well-known Gibbs-Thomson form [29], as a product of the local curvature and the surface stiffness (in 2D, $\gamma + d^2\gamma/d\theta^2$ with θ being the surface orientation). In the formalism of the phase-field model, and introducing the Willmore corner-regularization term [29,35] to deal with strong-anisotropy conditions, we get

$$\begin{aligned} \frac{\delta F}{\delta \varphi} = & -\epsilon \nabla \cdot [\gamma(\hat{\mathbf{n}})\nabla \varphi] + \frac{1}{\epsilon} \gamma(\hat{\mathbf{n}})W'(\varphi) \\ & - \nabla \cdot \left[\left(\frac{\epsilon}{2} |\nabla \varphi|^2 + \frac{1}{\epsilon} W(\varphi) \right) \nabla_{\nabla \varphi} \gamma(\hat{\mathbf{n}}) \right] \\ & + \beta \left[-\nabla^2 \kappa + \frac{1}{\epsilon^2} W''(\varphi) \kappa \right], \end{aligned} \quad (2)$$

with $W(\varphi) = 18\varphi^2(1-\varphi)^2$ being a double-well potential, $\kappa = -\epsilon \nabla^2 \varphi + (1/\epsilon)W'(\varphi)$ being the curvature, and β being a coefficient setting the strength of the corner rounding (here, $\beta = 0.01$).

In order to define the anisotropy for $\gamma(\hat{\mathbf{n}})$, $\tau(\hat{\mathbf{n}})$, and $\Phi(\hat{\mathbf{n}})$ we use the definition of Ref. [36]:

$$f(\hat{\mathbf{n}}) = f_0 \left[1 + \sum_i f_i(\hat{\mathbf{n}} \cdot \hat{\mathbf{m}}_i)^w \Theta(\hat{\mathbf{n}} \cdot \hat{\mathbf{m}}_i) \right], \quad (3)$$

where f stands for either γ , τ , or Φ ; $\{\hat{\mathbf{m}}_i\}$ is the set of orientations corresponding to the extremal points (minima or maxima) of the function; w is a parameter inversely proportional to the width of each peak; and Θ is the Heaviside step function.

Here, we simulate the evolution of a profile mimicking the one emerging over the dielectric mask from an arbitrary ring-shaped slit as in SAE, extending both laterally and vertically during deposition. Physically, two sources of material supply are to be considered: the direct impingement from the gas or liquid phase, with a distribution of precursors depending on the growth technique [e.g., molecular beam epitaxy (MBE) or metal organic chemical vapor deposition (MOCVD)]; and the lateral flow of material collected on the dielectric mask and diffusing along it before desorption. Generally, these processes may differ from one facet to another thus leading to anisotropic net deposition rates $\Phi(\hat{\mathbf{n}})$ being expected to play a major role at low temperatures (i.e., slow diffusion) or under reaction-limited growth conditions. Additional non-local effects, such as directionality in the gas supply or flux shielding effects between nearby structures can make the flux highly nonuniform. These will not be taken into account in

the following as they are specific to the experimental setup and pattern geometry.

For the sake of convenience, we take the case of wurtzite (WZ) InP reported in Ref. [10] as a reference for defining the set of facets, even though all considerations remain valid in general. This choice has the neat advantage of reducing the system geometry to a nearly two-dimensional (2D) one since, by taking the (0001) c plane as the substrate, the characteristic facets $\{10\bar{1}0\}$ (m planes) and $\{11\bar{2}0\}$ (a planes) are exactly perpendicular to it. Then, in a first approximation we can decouple the profile evolution in the (0001) basal plane while neglecting the height increment of the top facet, moving along the third direction. This justifies the effective use of 2D simulations, which will be extensively considered in this paper thanks to their low computational cost. Full three-dimensional (3D) simulations will be exploited for a more comprehensive description and for a validation of the 2D simulations. It will be shown in Sec. III B that a better reproduction of the actual behavior of 3D rings by 2D simulations is possible by admitting a larger flux on the inner side, $\Phi_{\text{in}} > \Phi_{\text{out}}$.

Zero-flux Neumann boundary conditions are considered in all cases. Since 3D simulations explicitly include the substrate surface as the bottom boundary of the simulation cell, a Neumann boundary condition is there imposed as in Ref. [37], so as to enforce a nonwetting boundary condition, mimicking the effect of the dielectric mask. An arbitrary large contact angle of 150° is here taken.

Growth simulations are performed by numerical integration of the PDE system of Eqs. (1) and (2) using the finite-element-method toolbox Adaptive Multidimensional Simulations (AMDiS) [38,39]. A semi-implicit time-integration scheme and adaptive mesh refinement are exploited to minimize the computational cost. The system size is physically set in nanometer units, so that simulations tackle the physical size of ring structures in experiments (up to a few micrometers in diameter), using $\epsilon = 10$ nm and a mesh resolution of 1 nm in 2D and 2.5 nm in 3D. The time unit is left arbitrary for the sake of generality. For the simulation of the more realistic cases in Secs. III B and III C, we set $\gamma_0/\tau_0 = 1$ arb. units and $\Phi_{\text{in}}/M_0 = 0.03$ arb. units, $\Phi_{\text{out}}/M_0 = 0.11$ arb. units ($\Phi/M_0 = 0.1$ arb. units elsewhere) in 2D, and $\gamma_0/\tau_0 = 0.5$ arb. units and $\Phi/M_0 = 8$ arb. units in 3D.

III. RESULTS AND DISCUSSION

A. Thermodynamic versus kinetic faceting

ECS and KCS can be considered as the reference cases toward which a growing crystal tends according to thermodynamics and kinetics, respectively. In Figs. 1(a) and 1(b), we sketch their difference for a ring structure. In Fig. 1(a) we consider anisotropic γ traced in the polar plot, with six equivalent minima, identified for convenience as the m planes of the WZ structure. The resulting ECS is given by the exposure of six such facets both in the inner and outer perimeter of the ring, as this corresponds to the lowest-energy morphology. In Fig. 1(b), facet-dependent growth velocities are considered by taking the six m planes as slow-growing facets and the six a planes at intermediate angles as fast-growing facets. These can be enforced either by anisotropic deposition flux

Φ or by considering anisotropy in the incorporation time τ as chosen in the figure (maxima in τ correspond to minima in facet velocity). The resulting KCS is characterized by an opposite faceting of the outer convex perimeter, set by the slow m planes, with respect to the inner concave perimeter, set by the fast a planes.

The formation of the ECS and KCS for a crystal with a different initial shape, imposed in SAE by the window geometry, is a dynamical process resulting from the balance between the supply of material by deposition and its redistribution by diffusion. As both processes have their own timescale, the faceting transition only occurs after a certain thickness is grown, as detailed in Ref. [30]. Notably, the faceting induced by γ and τ anisotropy results from surface diffusion dynamics, while the faceting due to flux anisotropy is not. Low Φ -to- M ratios favor energetic-driven faceting, while increasing the ratio enhances the role of incorporation kinetic anisotropy. Still, by further increasing the Φ -to- M ratio, flux anisotropy effects become dominant, outruling any diffusion effect.

In Figs. 1(c) and 1(d) the profile evolution of a circular slit during growth by isotropic deposition is traced for the two limiting cases of a fully thermodynamic regime [i.e., anisotropic γ and $\tau = 0$ in Eq. (1)] and a fully kinetic regime (i.e., anisotropic τ and isotropic γ). The simulation offers insight into the diffusion-driven kinetic pathway resulting, in the long run, in the expected ECS and KCS morphologies. In particular, in the early stages of the evolution in Fig. 1(c), short $\{11\bar{2}0\}$ facets appear even though excluded from the ECS. This comes from the definition of the $\gamma(\hat{\mathbf{n}})$ function, where small local minima [1/10 of those along the $\langle 10\bar{1}0 \rangle$ directions, barely visible in the polar plot of Fig. 1(a)] were defined along the $\langle 11\bar{2}0 \rangle$ directions, accounting for the fact that a planes could be stable facets even if ruled out by m planes in the present case. With the current definition, a planes are thermodynamically more convenient than the nearby orientations in the initial circular profile, so they develop locally at first but soon disappear because of the competition with the more favorable neighboring m planes.

From a general point of view, thermodynamic and kinetic contributions are expected to coexist and compete during the growth [30]. In Fig. 2(a), we enable both anisotropy in $\gamma(\hat{\mathbf{n}})$ and anisotropy in $\tau(\hat{\mathbf{n}})$, as set in the previous cases of Fig. 1, and inspect the change in the crystal morphology when changing their relative strength, by a variation in the scaling factor τ_0 , while keeping constant γ_0 . As expected, the faceting in the outer convex perimeter remains the same, because $\{10\bar{1}0\}$ m planes are set by construction as minima of γ as well as maxima of τ . Conversely, a transition in the faceting of the inner region is observed, going from a fully thermodynamic $\{10\bar{1}0\}$ faceting for the smallest τ_0 (0.1) to a mostly kinetic $\{11\bar{2}0\}$ faceting for the largest (1.0).

In the former case, the need of exposing low-energy facets is so strong that it hinders the advancing of the fast $\{11\bar{2}0\}$ fronts. In the latter, the incorporation on $\{11\bar{2}0\}$ is so fast that it suppresses any redistribution driven by energetics, thus forcing the exposure of the unfavorable facets. Interestingly, the length ratio between a and m planes decreases as the growth proceeds, i.e., as the inner region is filled and the perimeter shrinks. This is particularly evident in the case of $\tau_0 = 0.2$,

which is characterized at first by larger $\{11\bar{2}0\}$ segments, vanishing in the last stages as they are replaced by the most stable $\{10\bar{1}0\}$ planes.

Deeper insight into the dynamical process responsible for the observed faceting can be achieved by monitoring the temporal evolution of the chemical potential μ along the surface profile. The plots in Fig. 2(b) report the behavior of μ along the inner ring profile, for each of the four cases of τ_0 discussed above, at two representative growth stages, one representative of the initial faceting of the circular ring and the other showing the competition between the established facets at later stages. Profiting from the 12-fold symmetry of the anisotropic function, only the periodic sector between $\langle 10\bar{1}0 \rangle$ and $\langle 11\bar{2}0 \rangle$ directions is considered, and the actual values of μ are taken as the average of the equivalent points along the simulated profile to filter out the imperfect symmetry due to the mesh discretization. In all cases the chemical potential is continuous throughout the whole profile, with a smooth transition from one facet to another. Correspondingly, a continuous material flow $\mathbf{J} \sim -\nabla\mu$ is established along the surface, directed from the center of facets at higher μ towards adjacent facets at lower μ , altering their relative growth rates while still preserving the sharply faceted morphology at all evolution stages.

At the earliest time (0.5 arb. units), right after the quick reshaping of the initially circular ring profile by both m and a planes, a net material transfer is established between them, so that one extends at the expense of the other. For $\tau_0 = 0.1$, i.e., the case where thermodynamics is stronger, the current flows from the unfavored $\{11\bar{2}0\}$ kinetic facet toward the minimum- γ $\{10\bar{1}0\}$ ones, which grow larger from the beginning thanks to this additional flux. Vice versa, in all the three other cases ($\tau_0 = 0.2, 0.4$, and 1.0) the flow happens in the opposite direction since the $\{11\bar{2}0\}$ kinetic facets are favored over the most stable $\{10\bar{1}0\}$ ones by the increased τ_0 values. The greater is τ_0 , the stronger is the material current enhancing the relative growth rate of the $\{11\bar{2}0\}$ facets, which therefore grow larger.

However, this behavior reverts later on as indicated by the plots at time 2 arb. units. There, the minimum and maximum of μ are exchanged between the two facets thus driving material currents in the opposite direction. This is well evident in the cases for $\tau_0 = 0.2, 0.4$, and 1.0 , where material is transferred from $\{11\bar{2}0\}$ facets onto the energetically favored $\{10\bar{1}0\}$ ones, reflecting the increment in the strength of the thermodynamic contribution, proportional to the local curvature given by the Gibbs-Thomson relation, within the definition of the local μ . The reversal in the current causes an increment in the growth rate, and hence in size, of the thermodynamic $\{10\bar{1}0\}$ facets, resulting in the observed reduction of the a -plane-to- m -plane length ratio. A slightly different situation concerns the case for $\tau_0 = 0.1$, where the kinetic $\{11\bar{2}0\}$ facets are no longer present, replaced by slightly rounded corners that receive material by surface diffusion in order to coherently follow the advancing of the $\{10\bar{1}0\}$ facets. An analogous material flow toward facet edges is observed in the outer region (see Fig. S1 of the Supplemental Material [40]), where the corners between the $\{10\bar{1}0\}$ facets correspond to local minima of the chemical potential attracting some material to keep the pace of the advancing faceted front.

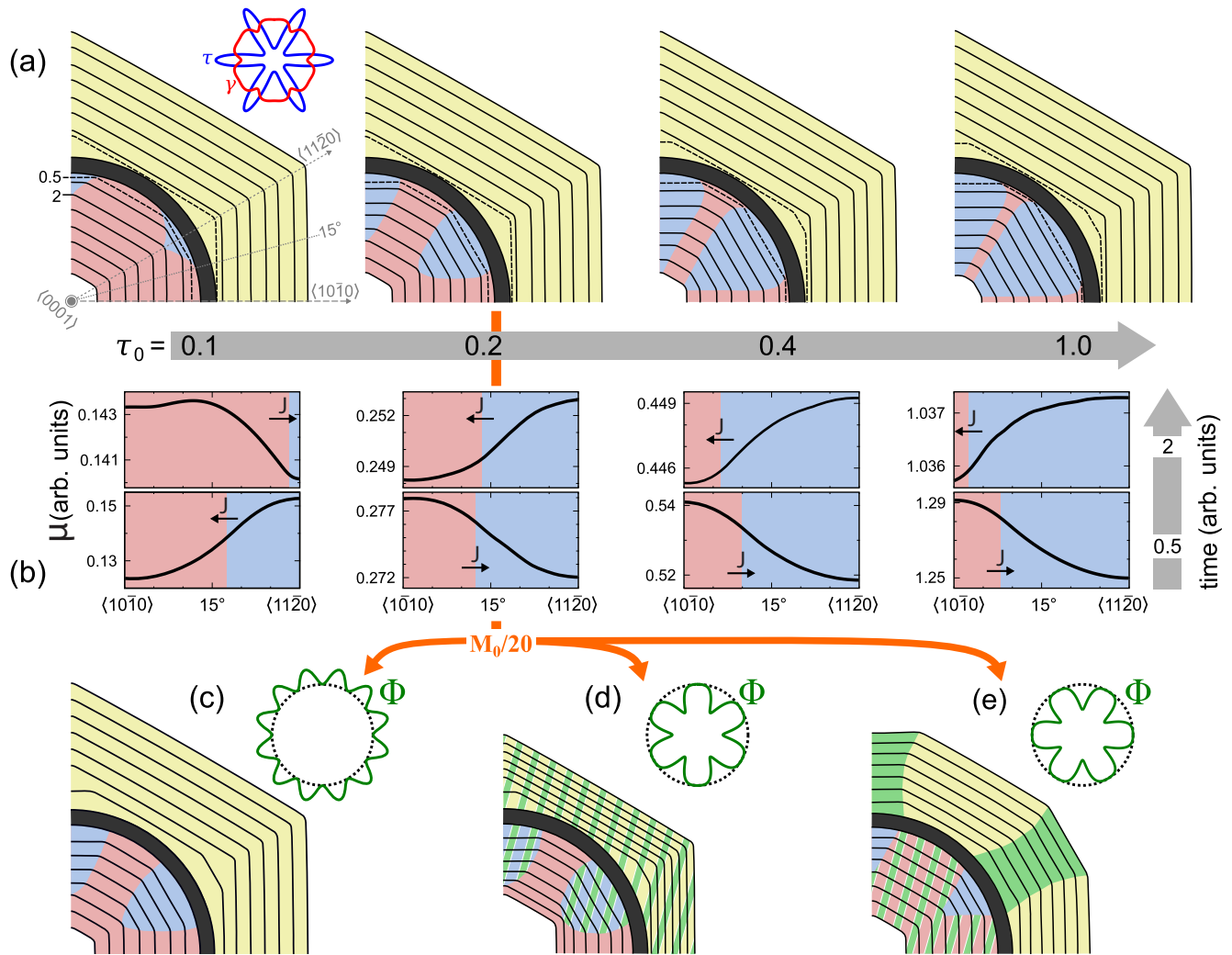


FIG. 2. (a) Evolution of a circular ring (black) during growth by a isotropic deposition flux in the presence of both anisotropic γ and τ , defined as in the polar plot and scaled according to the factor τ_0 (for fixed $\gamma_0 = 1$). Profiles are equally spaced in time except for the first (dashed lines), which corresponds to a half time interval. Regions are colored according to the thermodynamic (red), kinetic (blue), or mixed (yellow) driving force for the local faceting. Only a quarter of the ring is shown. (b) Plots of the chemical potential along the inner surface for the first and third growth profiles (growth time of 0.5 and 2 arb. units, respectively) in (a). Data are averaged in the periodic sectors between consecutive $\langle 10\bar{1}0 \rangle$ and $\langle 11\bar{2}0 \rangle$ directions, and the respective facets are distinguished by colors. (c)–(e) Same as the case for $\tau_0 = 0.2$ in (a) but including anisotropic deposition flux Φ with minima along both $\langle 10\bar{1}0 \rangle$ and $\langle 10\bar{2}0 \rangle$ (c), only along $\langle 10\bar{1}0 \rangle$ (d), and only along $\langle 11\bar{2}0 \rangle$ (e), as reported by the polar plots. Surface mobility is reduced by a factor of 20 to enhance the role of deposition with respect to diffusion. Regions are colored as in (a), and in green are indicated those affected by the deposition flux anisotropy alone (solid green regions) or combined with other driving forces (alternating bands).

Following this, it is worth noting how the current flow is again different between the outer convex profile and the inner concave one depending on the dominant driving force. In a thermodynamic regime, material flows from stable to unstable orientations in the convex region and in the opposite direction in the concave one. Once the equilibrium shape is established, the profile remains self-similar by pushing the required materials to the corners. In the kinetic regime, in contrast, the direction of material currents is the same for the convex and concave region, from those with slow incorporation dynamics to those where growth is faster, so that the former will extend on the outer perimeter due to their slow advancing while the latter will expand on the inner one as it is moving fast.

While the analysis here reported has been conducted by directly varying the kinetics-energetics balance by controlling the τ -to- γ ratio, rather similar effects (see Fig. S2 of the Supplemental Material [40]) can be achieved by tuning the flux-mobility (Φ/M) balance. It is indeed possible to see from Eq. (1) how an increment in the deposition rate returns a shift in μ from the equilibrium value and a consequent imbalance in favor of kinetic effects. This becomes even more important when the flux Φ is itself anisotropic thus entering the competition for the faceting by biasing the local supply of adatoms in each facet without involving any diffusion dynamics and irrespective of the local μ . In Figs. 2(c)–2(e) the very same case shown in Fig. 2(a) for $\tau_0 = 0.2$ is taken as a reference; however, the mobility M_0 is reduced by a factor of 20, and

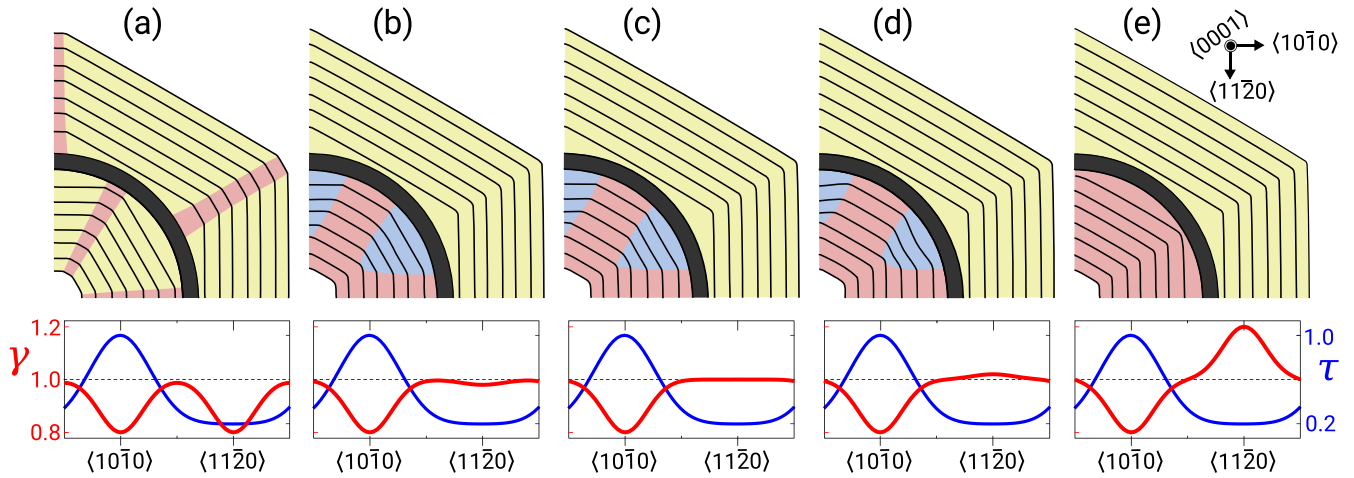


FIG. 3. (a)–(e) Simulation profiles of the evolution of a circular ring (black) during growth for different values of $\gamma_{\langle 11\bar{2}0 \rangle}$. Profiles are equally spaced in time, and regions are colored according to the thermodynamic (red), kinetic (blue), or mixed (yellow) driving force for the local faceting. Only a quarter of the ring is shown.

an anisotropic flux $\Phi(\hat{n})$ is considered, for the three most representative cases.

In Fig. 2(c), both $\{10\bar{1}0\}$ and $\{11\bar{2}0\}$ facets are assumed as identical minima of Φ , with the same magnitude as the reference flux Φ_0 used in the isotropic cases of Fig. 2(a), while the intermediate orientations are maxima. The obtained profile evolution is barely distinguishable from the one in Fig. 2(a) and practically the same if using the same mobility in the isotropic case (see Fig. S3 of the Supplemental Material [40]). This is due to the choice of flux anisotropy that does not produce any bias between the two facets, which is still enforced, and hence controlled in the relative extensions, by the anisotropy in γ and τ . More precisely, in the outer convex profile the reduced flux along the $\langle 10\bar{1}0 \rangle$ and $\langle 11\bar{2}0 \rangle$ directions favors the formation of both facets in the same way, while in the inner concave region it opposes their formation but is outruled by the other terms.

In Fig. 2(d), the flux along the $\langle 10\bar{1}0 \rangle$ directions is reduced to 1/2 of that along the $\langle 11\bar{2}0 \rangle$ ones, kept at the same magnitude as Φ_0 . In this case, the reduction in the adatom supply on the $\{10\bar{1}0\}$ facets adds to their already assumed stability (lower γ) and slow incorporation by τ anisotropy thus further enforcing their dominance in the outer convex perimeter, which now advances at 1/2 of the velocity of the isotropic case. Also in the inner concave region the behavior remains quite similar to the case of isotropic flux as the relative extension of $\{10\bar{1}0\}$ and $\{11\bar{2}0\}$ results from the relative strength of the kinetic contribution, here resulting from the combined effect of deposition and incorporation anisotropy, favoring the fast $\{11\bar{2}0\}$ front, and the thermodynamic driving force from surface energy, favoring the most stable $\{10\bar{1}0\}$ facets and becoming dominant only at small radii. The overall velocity of the inner growth front is also reduced, with a progressive slowdown as the relative extension of the $\{10\bar{1}0\}$ facets increases.

A different faceting can instead be obtained when considering the opposite case of minimum flux Φ in the $\langle 11\bar{2}0 \rangle$ directions, reported in Fig. 2(e). In such a case, the flux

anisotropy is opposite to the kinetic faceting by τ anisotropy, so that the slow arrival of material on $\{11\bar{2}0\}$ facets can compensate their fast incorporation capacity thus resulting in a significant slowdown of their motion compared with the case of isotropic deposition. For this reason, $\{11\bar{2}0\}$ facets can persist, and eventually prevail for thicker growth, on the outer perimeter as it is kinetically stabilized. Symmetrically, in the concave region the higher flux on $\{10\bar{1}0\}$ facets adds to the thermodynamic contribution by γ in driving their expansion against the $\{11\bar{2}0\}$ ones. A decrease in radial velocity is still observable on both sides but less pronounced as the growth proceeds since a larger part of the exposed facets correspond to the ones with maximum Φ .

It must be, however, pointed out that the actual impact of the flux anisotropy on the crystal faceting is directly controlled by the surface mobility. In the cases reported in Figs. 2(c)–2(e), the surface diffusion has been significantly quenched by setting a low mobility so as to limit the redistribution of the deposited material according to the nonuniform μ and obtain facet growth rates mainly defined by the different local supply. If the mobility is increased (see Fig. S3 of the Supplemental Material [40]), the effects of an uneven supply of material by anisotropic flux Φ become less and less important as adatoms redistribute along the surface profile following the μ gradients. In the following we will focus on the latter regime, assuming that, for the typical conditions of the experimental cases here considered, the diffusion is fast enough to neglect the possible, reasonably small, anisotropy in the deposition flux.

In Fig. 3 we investigate the effect of changing the energetics of the $\{11\bar{2}0\}$ a planes, while leaving the incorporation time τ unchanged, for the intermediate regime of $\tau_0 = 0.2$ in Fig. 2(a), here repeated for convenience in Fig. 3(b). In the case shown in Fig. 3(a), minima as deep as the $\{10\bar{1}0\}$ ones are considered, so that the ECS is a regular dodecagon. However, the adatom kinetics introduces a bias between the two facet families: In the outer perimeter, the slower $\{10\bar{1}0\}$ facets dominate, and in the inner one the fast $\{11\bar{2}0\}$ facets

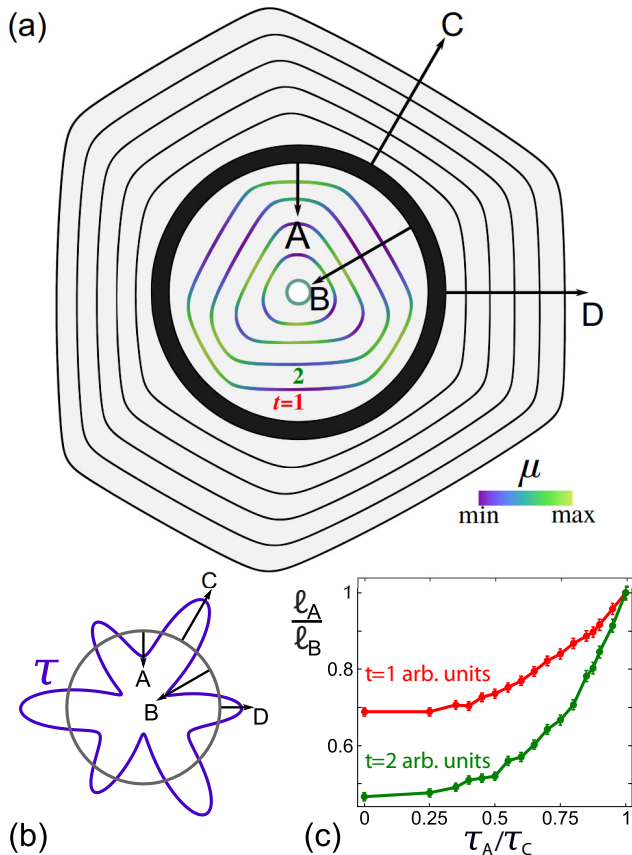


FIG. 4. Growth of a ring with multiple facet families defined in the kinetic term. (a) The initial ring is colored black, and growth profiles equally spaced in time are drawn. The chemical potential is mapped independently for each profile in the concave region. Four facet families with different growth velocities are distinguished. (b) Polar plot of the kinetic term. The same facet families are highlighted. (c) Ratio of the lengths of facets A and C plotted against the ratio of the respective incorporation times. Only the first two growth profiles are considered. In order to reduce the error, the average length over each facet family at the respective time frame was used.

grow larger. In Fig. 3(e), the opposite situation is defined, with maxima of γ along the $\langle 11\bar{2}0 \rangle$ directions, resulting in $\{10\bar{1}0\}$ hexagonal profiles in both the inner and outer perimeters. While both thermodynamic and kinetic contributions push the system in this same direction in the outer profile, in the concave part the faceting is enforced by the energetic term, opposing the exposure of the highest-energy $\{11\bar{2}0\}$ planes despite their fast incorporation rate. The intermediate case shown in Fig. 3(c) with constant value of γ along the $\langle 11\bar{2}0 \rangle$ directions results, in the early growth stages, in the coexistence of $\{10\bar{1}0\}$ planes, energetically favored because they are minima in γ , and $\{11\bar{2}0\}$ planes, which are characterized by a lower incorporation time τ with respect to nearby orientations at the same energy. As already seen in Fig. 2(a), as the perimeter shrinks, thermodynamic effects prevail, as highlighted by the reversal of the μ gradients along the profile, so that at the latest growth stages the profile reduces to the energetically favored $\{10\bar{1}0\}$ facets. Finally, the cases in Figs. 3(b) and 3(d) show the effect of setting shallow minima or maxima,

respectively, along the $\langle 11\bar{2}0 \rangle$ directions, as small as $1/10$ of the absolute minima along $\langle 10\bar{1}0 \rangle$. The behavior is quite similar to the behavior with constant γ in Fig. 3(c), but a difference is observed in the relative extension of the $\{11\bar{2}0\}$ facets, longer in Fig. 3(b) than in Fig. 3(d), and, in turn, in the deposited thickness at which they disappear.

So far we have focused on variations in the faceting due to the competition between facets differently favored by thermodynamics and kinetics. We now turn our attention to the case where more than one facet family can appear in the kinetic regime. More precisely, here we investigate how the morphology of the crystal changes in both the inner and outer region when considering different maxima and minima for the facets. An exemplifying case is illustrated in Fig. 4, where, to keep the analysis as simple as possible, we still consider the same geometry as before but we assume two different maximum values for the incorporation time of alternating $\{10\bar{1}0\}$ planes, labeled A and C, with $\tau_A > \tau_C$, and two minimum values for the $\{11\bar{2}0\}$ planes, labeled B and D, with $\tau_B > \tau_D$. The polar plot of $\tau(\hat{n})$ is shown in Fig. 4(b). The overall criterion of KCS still holds: In the convex outer perimeter the slowest-growing facet, i.e., the C facet, prevails, while in the concave inner profile it is the fastest one, i.e., the B facet, that dominates. However, the evolution proceeds through intermediate stages where the relative facet extension changes continuously, on a timescale determined by the diffusion-to-growth ratio and controlled by the difference in the incorporation times. In Fig. 4(c) the variation in the ratio of the facet lengths ℓ for the two families A and B as a function of the ratio in their incorporation times is plotted for two simulation stages, corresponding to the first and second profiles in Fig. 4(a). As expected, for the same incorporation time, both facets coexist with the same extension, producing a hexagonal profile. The larger the difference between the incorporation times, the stronger the driving force for the facet transition, corresponding to a difference in the chemical potential, higher for facet A and lower for facet B. This kinetic effect would cause a triangle with A facets only to form in the concave region. However, the kinetic faceting is once again found to produce sharp facets only for a sufficiently large radius. When the inner perimeter shrinks, as made evident in the latest stages of Fig. 4(a), the chemical potential at the corners increases due to their high curvature energy cost, thus driving a local rounding that, in the end, results in a nearly circular morphology right before the full closure of the hole.

B. Simulation of realistic ringlike structures

Since all of the previous analysis considered a 2D geometry, questions may arise as to how it applies to realistic 3D structures. Two major differences are to be taken into account. First, the inner and outer regions are no longer fully decoupled as the crystal top facet connects them. Second, the explicit representation of the lateral growth on top of the substrate requires us to introduce an appropriate boundary condition to enforce the nonwetting contact angle on the dielectric mask. In Fig. 5 we consider a fully 3D simulation with incorporation anisotropy only, mimicking the experimental behavior of the ring structures in Ref. [10]. To this purpose, both m and a planes, observed in the outer profile, are to be considered

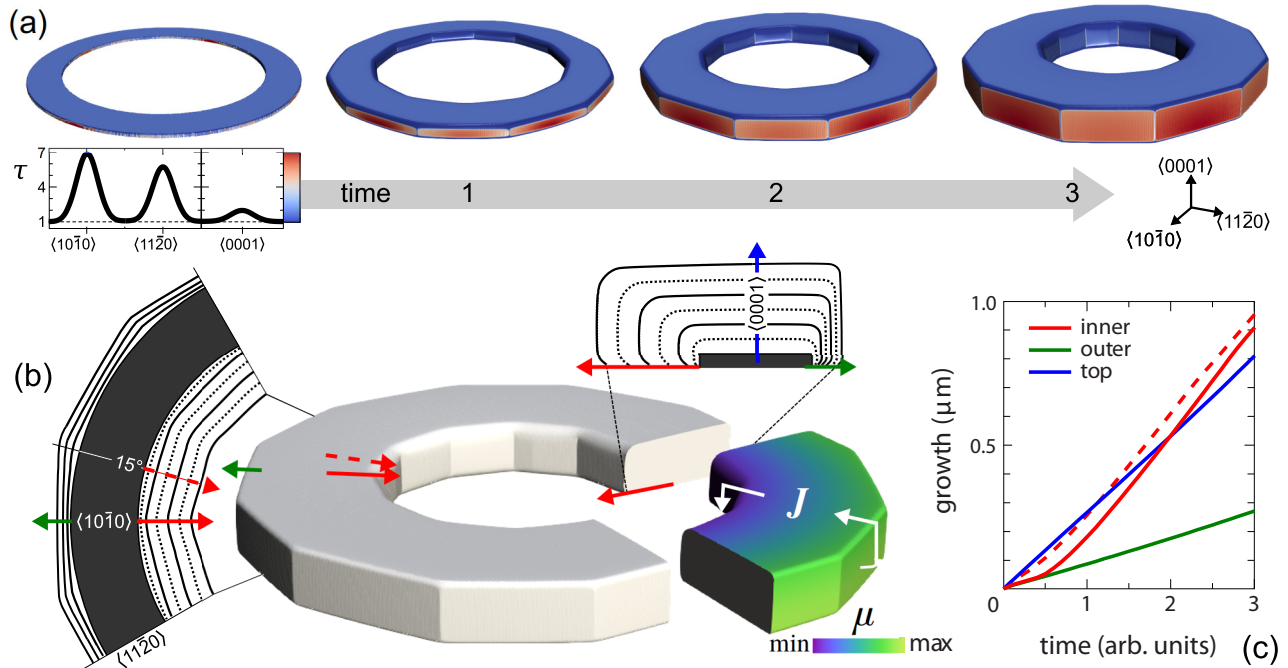


FIG. 5. (a) 3D simulation growth stages of a ring geometry with an external diameter of 800 nm. Color maps represent the value of τ , whose angular variation is schematized in the inset. (b) Profile sequences for two cross sections, namely, on the (0001) and $\{10\bar{1}0\}$ planes, and color map for the surface chemical potential μ for the last stage of (a), sketching the current of material J . (c) Variation with time of the lateral and vertical growth of the structure. Each line reports the evolution in the corresponding direction identified by the arrows in (b).

as maxima of τ while leaving all 12 intermediate directions, angled at 15° with respect to $\langle 10\bar{1}0 \rangle$ and $\langle 11\bar{2}0 \rangle$, as identical minima, so that they develop equally in the concave region. A satisfactory agreement with the experimental observations is achieved by taking $\tau_{10\bar{1}0} : \tau_{11\bar{2}0} : \tau_{0001} : \tau_0 = 6 : 5 : 1 : 1$, as sketched in the figure inset. The growth progress is illustrated in Fig. 5(a), where consecutive simulation stages are reported, starting from the initial circular ring on the left. A more in-depth analysis of the evolution of the growth front is reported

in Fig. 5(b), where the sequence of growth profiles is traced for both a vertical $\{11\bar{2}0\}$ cross section and in a (0001) top view. These highlight a major effect that could not be taken into account by a simple 2D model: The concave region grows much faster than the convex one. This is the consequence of a large material transfer driven by the difference in μ between the outer and the inner region, as seen in the color map in Fig. 5(b), from the slow-growing front in the outer perimeter (where τ and μ are maxima), onto the (0001) top facet, and then toward the fast-growing 15° facets on the concave side, where τ and μ are minima. More quantitatively, the different advancements of the growth front at the inner and outer perimeter and at the crystal top are plotted in Fig. 5(c).

Despite the qualitative resemblance of the simulation with the experimental images, the scale of the latter, about $4 \mu\text{m}$ in diameter, cannot be matched easily due to the high computational cost of 3D modeling. A one-to-one size reproduction could be achieved effortlessly by 2D simulations, provided that they properly approximate the evolution of the 3D system mapped in the substrate plane. As we just recognized that the advancing of the growth front is strongly asymmetric, a correcting factor is to be included in the 2D simulations in order to assign a different effective flux Φ on the two sides of the ring. Based on the measurements in Fig. 5(c), we set the flux ratio to $\Phi_{\text{in}} : \Phi_{\text{out}} = 11 : 3$. With this change, 2D results are found to reproduce well the cross-sectional evolution of 3D simulations, as shown in Fig. 6(a) for a small ring with diameter 400 nm, as well as for the profiles of the 800-nm ring considered in Fig. 5 (not shown). The good correspondence certifies the possibility of exploiting 2D as a quick and reasonably approximated description of the profile evolution, with the neat advantage

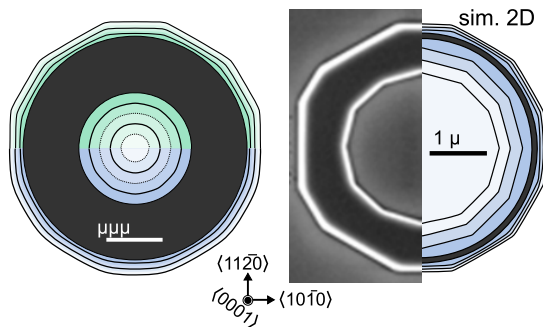


FIG. 6. (a) Comparison between the simulations (sim.) of growth of a ring in 3D (green) and 2D (blue). The initial ring is colored black, and growth profiles equally spaced in time are traced up until the closure of the cavity. (b) Comparison between the scanning electron microscopy (SEM) view of an InP ring from Ref. [10] and the corresponding 2D growth simulation. (SEM image is adapted with permission. Copyright 2021 American Chemical Society.) Simulated profiles are drawn equally spaced in time up to matching the experimental one.

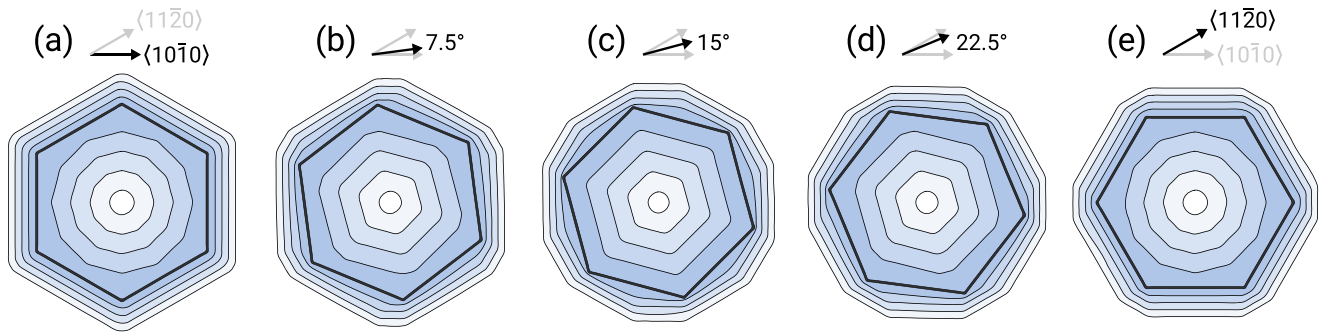


FIG. 7. (a)–(e) Growth simulations starting from a hexagonal pattern (black) at different angles. Growth profiles equally spaced in time are traced up until the closure of the cavity.

of tracking the evolution for much longer times and, even more critically, for much larger sizes, comparable to experimental ones. This is represented in Fig. 6(b), where a direct comparison between 2D simulation profiles and the experimental structure of Ref. [10] is shown to achieve substantial agreement.

C. Template effect

As the faceting process is essentially bounded to the finite timescale of the surface diffusion process, the crystal morphology can be controlled by engineering the shape of the initial profile, i.e., the geometry of the underlying slit for the SAE growth. In the previous analysis the most neutral profile possible, a circular unfaceted slit, has been considered, in order to let facets develop spontaneously. On the other hand, by exploiting a polygonal profile with a given orientation on the substrate plane, it is possible to introduce a bias in the facet formation, favoring those already present or closer to the initial profile. This is made evident, in 2D, in Fig. 7, where the initial profile is shaped like a hexagon with sides aligned

along different directions, ranging from $\langle 11\bar{2}0 \rangle$ in Fig. 7(a) to $\langle 10\bar{1}0 \rangle$ in Fig. 7(e). In Fig. 7(a), the outer profile grows conformally as the preset $\{10\bar{1}0\}$ planes correspond to the absolute maxima of τ , so that they are the most favored by kinetics, while in the inner region the dodecagonal profile set by the 15° facets is seen until the closure of the cavity. In the case shown in Fig. 7(e), the evolution is quite similar, but, since the preset $\{11\bar{2}0\}$ planes are only relative maxima of τ , they get slowly replaced by the most convenient $\{10\bar{1}0\}$ facets developing from the corners of the initial hexagon. The very same templating effect, but referred to the inner region, is observed in the case shown in Fig. 7(c), where the sides of the initial hexagon are aligned with the 15° fast-growing facets. In this case, only six such orientations, out of the 12 existing ones, are observed, and the growth is conformal until the full closure of the cavity. On the other hand, the initial orientation does not match any of the favorable m or a planes on the outer side, so that a rapid, complete rearrangement in the profile is observed, leading to the exposure of both favorable families. As the hexagon sides are exactly in the middle between the two, the $\{10\bar{1}0\}$ facets tend to grow slightly larger than the $\{11\bar{2}0\}$ ones, in the same way as the circular slit of Fig. 6. Finally, in Figs. 7(b) and 7(d) the initial profile is not aligned with any favorable orientations, either for the convex or for the concave profile. In this case, the profile undergoes an initial realignment to the $\langle 11\bar{2}0 \rangle$ and $\langle 10\bar{1}0 \rangle$ directions in the outer region and to the 15° intermediate facet in the inner one. During this process, the facets which are closest to the initial hexagon sides tend to prevail, so that in Fig. 7(b) the $\{10\bar{1}0\}$ facets extend the most, while in Fig. 7(d), which is rotated closer to the $\langle 10\bar{1}0 \rangle$ direction, the profile is first dominated by the $\{11\bar{2}0\}$ facets, with the most favorable $\{10\bar{1}0\}$ emerging later. Looking at the inner region, in both Figs. 7(b) and 7(d) the initial hexagon profile favors only six intermediate facets, while the others appear initially at the corners but are consumed before the closure of the cavity, thus returning a hexagonal perimeter. Notably, this indicates that the KCS will be eventually reached in all cases in the convex region, but the timescale required to do so is affected strongly by variations in the initial orientation of the pattern. This may be more critical in the inner region, as in principle the cavity may close before a steady state is reached.

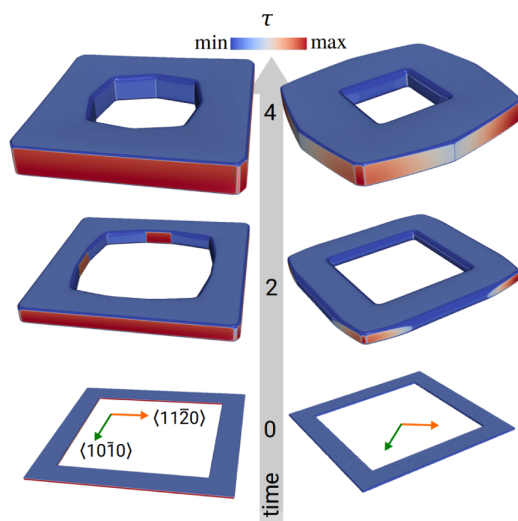


FIG. 8. Growth sequences for two different orientations of the initial squared ring. (left) The sides of the initial square are made of two $\{10\bar{1}0\}$ and $\{11\bar{2}0\}$ facets. (right) Same initial shape as in the left column, but rotated 45° on the (0001) substrate. The external side of the initial shape is 800 nm long.

The possibility of controlling the patterning with high precision offered by the current lithographic techniques allows for arbitrary slit shapes, not necessarily reflecting the substrate

symmetry. In Fig. 8 a squared ring is considered, and its evolution during growth is investigated by 3D simulations for two different orientations. In the case shown on the left in Fig. 8, the sides of the square are aligned two by two with $\{10\bar{1}0\}$ and $\{11\bar{2}0\}$ facets, so that the outer profile remains quite the same except for the nucleation of the four missing $\{10\bar{1}0\}$ facets at the square corners. In the inner region, the growth starts with the accumulation of material at the corners, forming 15° facets, progressively extending toward the center of the edges so as to replace the slow m and a planes of the initial square. The effect of the template is, however, evident as only the eight fast-growing planes at 15° with respect to the initial square sides are formed, while the remaining four planes expected at the corners of the square are not observed. In the case shown on the right in Fig. 8, the initial square is rotated by 45° so that all facets correspond to fast-growing fronts at 15° with respect to the m and a planes. As expected, this alignment is preserved in the inner concave region, while in the outer perimeter the slow-growing planes nucleate, starting from the corners. However, as the growth of the concave region is much faster, only a local rearrangement of the profile is found in the outer region before the closure of the inner cavity.

IV. CONCLUSIONS

The complex dynamics of crystal growth of ringlike structures was investigated by phase-field simulations. The coexistence of convex and concave regions almost decoupled from each other, i.e., the inner and outer perimeter of the ring, offers a valuable strategy to assess the relative role of thermodynamics and kinetics in driving the crystal faceting, for the nucleationless growth mode. Our analysis shows that a continuous variation in the morphology between the extreme cases of ECS and KCS is possible as a function of the relative strength of anisotropic surface energy, incorporation kinetics, and orientation-dependent deposition flux or through the Φ -to- M ratio.

Importantly, our approach not only returns the final morphology, but also tackles the full kinetic pathway driving the

system from the initial shape, templated by the window slit in SAE, across all intermediate stages before the final one. The comparison of our simulation results with experimental cases in the literature, in particular, with the case of InP rings here taken as reference, shows the consistency of the modeling and indicates a major role of kinetics in leading the faceting of crystals grown by SAE. While the present study was not meant to be a quantitative comparison of specific experiments, the proposed approach could be used as a more predictive tool, by a suitable calibration of the parameters, following the approach proposed in Ref. [21] for nanomembranes. To this purpose, the comparison and validation of the model setup against experimental time series would be quite necessary, especially for the fine-tuning of the facets' incorporation times, generally unknown and difficult to achieve by theoretical calculations. With this respect, the possibility of exchanging the fully representative, but more demanding, 3D simulations for an effective 2D description extends the size scale and timescale accessible by simulations making a one-to-one comparison with micrometer-sized structures possible.

Finally, the implicit representation of the geometry in the phase-field approach makes it possible to consider any arbitrary shape of the mask windows as initial profiles, so that simulations can be used for scouting new growth designs in place of running expensive experimental campaigns. Indeed, once the parameters are properly set they can be straightforwardly used for simulating different window shapes and crystallographic alignments, as well as different substrate orientations. This offers a great advantage in the tuning of the crystal morphology, as the window shape can template the faceting during the earliest growth stages.

ACKNOWLEDGMENTS

We gratefully thank M. Salvalaglio for fruitful discussions. We acknowledge the CINECA award under the ISCRA initiative, for the availability of high-performance-computing resources and support.

-
- [1] X. Yuan, D. Pan, Y. Zhou, X. Zhang, K. Peng, B. Zhao, M. Deng, J. He, H. H. Tan, and C. Jagadish, *Appl. Phys. Rev.* **8**, 021302 (2021).
 - [2] X. Mei, D. Kim, H. E. Ruda, and Q. X. Guo, *Appl. Phys. Lett.* **81**, 361 (2002).
 - [3] A. Winden, M. Mikulics, A. Haab, T. Stoica, M. von der Ahe, K. Wirtz, H. Hardtdegen, and D. Grützmacher, *Phys. Status Solidi C* **9**, 624 (2012).
 - [4] K. Tomioka, K. Ikejiri, T. Tanaka, J. Motohisa, S. Hara, K. Hiruma, and T. Fukui, *J. Mater. Res.* **26**, 2127 (2011).
 - [5] X. Wang, S. Li, S. Fündling, J. Wei, M. Erenburg, H.-H. Wehmann, A. Waag, W. Bergbauer, M. Strassburg, U. Jahn, and H. Riechert, *Cryst. Growth Des.* **12**, 2552 (2012).
 - [6] Ž. Gačević, D. Gómez Sánchez, and E. Calleja, *Nano Lett.* **15**, 1117 (2015).
 - [7] C.-Y. Chi, C.-C. Chang, S. Hu, T.-W. Yeh, S. B. Cronin, and P. D. Dapkus, *Nano Lett.* **13**, 2506 (2013).
 - [8] G. Tütüncüoğlu, M. de la Mata, D. Deiana, H. Potts, F. Matteini, J. Arbiol, and A. Fontcubertai Morral, *Nanoscale* **7**, 19453 (2015).
 - [9] J. Hartmann, F. Steib, H. Zhou, J. Ledig, S. Fündling, F. Albrecht, T. Schimpke, A. Avramescu, T. Varghese, H.-H. Wehmann, M. Straßburg, H.-J. Lugauer, and A. Waag, *Cryst. Growth Des.* **16**, 1458 (2016).
 - [10] N. Wang, X. Yuan, X. Zhang, Q. Gao, B. Zhao, L. Li, M. Lockrey, H. H. Tan, C. Jagadish, and P. Caroff, *ACS Nano* **13**, 7261 (2019).
 - [11] P. Aseev, A. Fursina, F. Boekhout, F. Krizek, J. E. Sestoft, F. Borsoi, S. Heedt, G. Wang, L. Binci, S. Martí-Sánchez, T. Swoboda, R. Koops, E. Uccelli, J. Arbiol, P. Krogstrup, L. P. Kouwenhoven, and P. Caroff, *Nano Lett.* **19**, 218 (2019).

- [12] J. S. Lee, S. Choi, M. Pendharkar, D. J. Pennachio, B. Markman, M. Seas, S. Koelling, M. A. Verheijen, L. Casparis, K. D. Petersson, I. Petkovic, V. Schaller, M. J. W. Rodwell, C. M. Marcus, P. Krogstrup, L. P. Kouwenhoven, E. P. A. M. Bakkers, and C. J. Palmstrøm, *Phys. Rev. Mater.* **3**, 084606 (2019).
- [13] P. Staudinger, K. E. Moselund, and H. Schmid, *Nano Lett.* **20**, 686 (2020).
- [14] P. Staudinger, S. Mauthe, N. V. Trivino, S. Reidt, K. E. Moselund, and H. Schmid, *Nanotechnology* **32**, 075605 (2021).
- [15] F. Krizek, J. E. Sestoft, P. Aseev, S. Marti-Sanchez, S. Vaitiekėnas, L. Casparis, S. A. Khan, Y. Liu, T. Stankevič, A. M. Whitar, A. Fursina, F. Boekhout, R. Kooops, E. Uccelli, L. P. Kouwenhoven, C. M. Marcus, J. Arbiol, and P. Krogstrup, *Phys. Rev. Mater.* **2**, 093401 (2018).
- [16] J. Winnerl, M. Kraut, S. Artmeier, and M. Stutzmann, *Nanoscale* **11**, 4578 (2019).
- [17] D. Du, D. J. Srolovitz, M. E. Coltrin, and C. C. Mitchell, *Phys. Rev. Lett.* **95**, 155503 (2005).
- [18] V. Jindal and F. Shahedipour-Sandvik, *J. Appl. Phys.* **106**, 083115 (2009).
- [19] Q. Sun, C. D. Yerino, B. Leung, J. Han, and M. E. Coltrin, *J. Appl. Phys.* **110**, 053517 (2011).
- [20] L. K. Agesen, M. E. Coltrin, J. Han, and K. Thornton, *J. Appl. Phys.* **117**, 194302 (2015).
- [21] M. Albani, L. Ghisalberti, R. Bergamaschini, M. Friedl, M. Salvalaglio, A. Voigt, F. Montalenti, G. Tütüncüoğlu, A. Fontcubertai Morral, and L. Miglio, *Phys. Rev. Mater.* **2**, 093404 (2018).
- [22] L. D. Marks and L. Peng, *J. Phys.: Condens. Matter* **28**, 053001 (2016).
- [23] G. Wulff, *Z. Kristallogr. Mineral.* **34**, 449 (1901).
- [24] J. W. Cahn and W. C. Carter, *Metall. Mater. Trans. A* **27**, 1431 (1996).
- [25] S. H. Jones, L. K. Siedel, and K. M. Lau, *J. Cryst. Growth* **108**, 73 (1991).
- [26] R. Bergamaschini, F. Isa, C. V. Falub, P. Niedermann, E. Müller, G. Isella, H. von Känel, and L. Miglio, *Surf. Sci. Rep.* **68**, 390 (2013).
- [27] T. Ma, W. Ren, X. Zhang, Z. Liu, Y. Gao, L. C. Yin, X. L. Ma, F. Ding, and H. M. Cheng, *Proc. Natl. Acad. Sci. USA* **110**, 20386 (2013).
- [28] X. Kong, J. Zhuang, L. Zhu, and F. Ding, *npj Comput. Mater.* **7**, 14 (2021).
- [29] B. Li, J. Lowengrub, A. Rätz, and A. Voigt, *Commun. Comput. Phys.* **6**, 433 (2009).
- [30] M. Albani, R. Bergamaschini, M. Salvalaglio, A. Voigt, L. Miglio, and F. Montalenti, *Phys. Status Solidi B* **256**, 1800518 (2019).
- [31] J. W. Cahn and J. E. Taylor, *Acta Metall. Mater.* **42**, 1045 (1994).
- [32] C. Gugenberger, R. Spatschek, and K. Kassner, *Phys. Rev. E* **78**, 016703 (2008).
- [33] M. Salvalaglio, A. Voigt, and S. M. Wise, *Math. Methods Appl. Sci.* **44**, 5385 (2021).
- [34] M. Salvalaglio, M. Selch, A. Voigt, and S. M. Wise, *Math. Methods Appl. Sci.* **44**, 5406 (2021).
- [35] S. Torabi, J. Lowengrub, A. Voigt, and S. Wise, *Proc. R. Soc. A* **465**, 1337 (2009).
- [36] M. Salvalaglio, R. Backofen, R. Bergamaschini, F. Montalenti, and A. Voigt, *Cryst. Growth Des.* **15**, 2787 (2015).
- [37] W. Jiang, W. Bao, C. V. Thompson, and D. J. Srolovitz, *Acta Mater.* **60**, 5578 (2012).
- [38] S. Vey and A. Voigt, *Comput. Visualization Sci.* **10**, 57 (2007).
- [39] T. Witkowski, S. Ling, S. Praetorius, and A. Voigt, *Adv. Comput. Math.* **41**, 1145 (2015).
- [40] See Supplemental Material at <http://link.aps.org/supplemental/10.1103/PhysRevMaterials.6.023401> for additional simulation data.